Attenuation of Plasmaspheric Hiss Associated with the Enhanced Magnetospheric Electric Field

Haimeng Li[1,2], Wen Li[2], Qianli Ma[3,2], Yukitoshi Nishimura[2], Zhigang Yuan[4], Alex J. Boyd[5,6], Xiaochen Shen[2], Rongxin Tang[1], and Xiaohua Deng[1]

[1] Institute of Space Science and Technology, Nanchang University, Nanchang, China
[2] Center for Space Physics, Boston University, Boston, MA, USA.
[3] Department of Atmospheric and Oceanic Sciences, University of California, Los Angeles, CA, USA.
[4] School of Electronic Information, Wuhan University, Wuhan, China
[5] New Mexico Consortium, Los Alamos, NM, USA
[6] Space Sciences Department, The Aerospace Corporation, Chantilly, VA, USA

Correspondence to: Haimeng Li (lihaimeng@ncu.edu.cn); Wen Li (luckymoon761@gmail.com)

Abstract. We report an attenuation of hiss wave intensity in the duskside of outer plasmasphere in response to enhanced convection and substorm based on Van Allen Probes observations. Using test particle codes, we simulate the dynamics of energetic electron fluxes based on a realistic magnetospheric electric field model driven by solar wind and subauroral polarization stream. We suggest that the enhanced magnetospheric electric field causes the outward and sunward motion of energetic electrons, corresponding to the decrease of energetic electron fluxes on the duskside, leading to the subsequent attenuation of hiss wave intensity. The results indicate that the enhanced electric field can significantly change the energetic electron distributions, which provide free energy for hiss wave amplification. This new finding is critical for understanding the generation of plasmaspheric hiss and its response to solar wind and substorm activity.

1 Introduction

Plasmaspheric hiss is a structureless, extremely low frequency (ELF) whistler mode wave that is found primarily in the plasmasphere (Russell et al., 1969; Thorne et al., 1973) and plasmaspheric plumes (Chan and Holzer, 1976; Parrot and Lefeuvre, 1986; Shi et al., 2019; Yuan et al., 2012). Hiss waves are broadband emissions with frequencies typically between 100 Hz and 2 kHz (Meredith et al., 2004; Thorne et al., 1973). However, recent studies indicate that hiss wave frequencies can extend below 100 Hz during strong substorm activities (W. Li et al., 2013, 2015a; H. Li et al., 2015; Ni et al., 2014). Hiss waves can scatter energetic electrons into the loss cone, thereby playing an important role in energetic electron dynamics in the radiation belt (Ma et al., 2016; Meredith et al., 2006, 2007, 2009; Su et al., 2011; Thorne et al., 2013). The mechanism of hiss wave generation is still under active research. Two main generation mechanisms have been proposed: (1) external origination: propagation effects of the whistler-mode chorus from the plasmatrough (Bortnik et al., 2008, 2009; W. Li et al., 2015b; Su et

1

al., 2015) or lightning generated whistler (Draganov et al., 1992; Green et al., 2005); (2) internal generation: excitation due to local electron cyclotron resonance instability inside the plasmasphere or plasmaspheric plume (Chen et al., 2014; Su et al., 2018; Summers et al., 2014; Thorne et al., 1979). Shi et al. (2019) suggest that the hiss waves in the outer plasmasphere tend to be locally amplified, whereas the hiss waves at the lower L shells may propagate from higher L shells. The Poynting flux of hiss directed away from the equator provides evidence of internal local generation of hiss waves (He et al., 2019; Kletzing et al., 2014; Laakso et al., 2015; Su et al., 2018). In contrast, the bidirectional Poynting flux of hiss waves implies that local electron instability is relatively weak and the observed hiss waves mainly originate from chorus waves (Liu et al., 2017a, 2017b).

A large-scale dawn-dusk convection electric field is produced in the inner magnetosphere due to the motional solar wind electric field ($\boldsymbol{E}_{SW} = -\boldsymbol{V} \times \boldsymbol{B}$), where $\boldsymbol{V}$ is the solar wind velocity and $\boldsymbol{B}$ is the interplanetary magnetic field (Lei et al., 1981). Since the $\boldsymbol{E}_{SW}$ is mapped along the geomagnetic field lines and penetrates into the magnetosphere (Huang et al., 2006; Toffoletto and Hill, 1989), Goldstein et al. (2005a) suggest that the electric field at the plasmapause was approximately 13% of E_{SW}. Besides the global contribution of E_{SW}, the ionospheric subauroral polarization stream (SAPS) is potentially an important contributor to the magnetospheric electric field near the duskside (Goldstein et al., 2003, 2005a, 2005b). The SAPS is the westward flow located at ~3-5° of magnetic latitude below the auroral oval near the duskside. The ionospheric SAPS electric field can be mapped to the magnetic equatorial plane as radial electric fields. In general, the SAPS is related to the substorm and intensifies within ~10 min after the substorm onset (Mishin et al., 2005). It has been known that the dawn-dusk convection electric field plays an important role in the motions of charged particles through the $\boldsymbol{E} \times \boldsymbol{B}$ drift, especially during strong geomagnetic activity (Burch, 1977; Ejiri, 1978; Frank, 1975). Using an improved electric field model driven by $\boldsymbol{E}_{SW}$ and SAPS, Goldstein et al. (2003) simulated the evolution of plasmapause location, which is found to be very similar to the plasmapause produced by the IMAGE extreme ultraviolet imager.

In this paper, we report an interesting event where plasmaspheric hiss intensity decreased associated with the enhanced convection and substorm activity on 27 August 2013. Using test particle simulations based on the realistic electric field model, we provide direct evidence that enhanced magnetospheric electric field can contribute to the attenuation of hiss wave intensity on the duskside.

2 Satellite data

The twin Van Allen Probes with perigee and apogee of about 1.1 and 5.8 R_E measure both hiss waves and energetic electron fluxes (Mauk et al., 2012). In this study, data from the Electric and Magnetic Field Instrument Suite and Integrated Science (EMFISIS) instrument are utilized to measure hiss waves (Kletzing et al., 2013), and the data from Electric Fields and Waves (EFW) instrument are utilized to measure electric fields (Wygant et al., 2013). Moreover, we use the data from Magnetic Electron Ion Spectrometer (MagEIS) and Helium Oxygen Proton Electron (HOPE) to analyze in situ energetic electron distributions (Blake et al., 2013; Funsten et al., 2013; Spence et al., 2013).

65 The Defense Meteorological Satellite Program (DMSP) satellites orbit around the Earth at an altitude of about 850 km and

66 measure the ion drift velocities in both horizontal and vertical directions perpendicular to the satellite orbit (Rich and Hairston,

67 1994). In this study, the data of DMSP F17 are used to identify the SAPS event. Furthermore, we use the 1-min resolution

68 OMNI data to analyze the solar wind parameters including the interplanetary magnetic field (IMF).

69 **3 Event overview**

70 Figure 1 shows the overview of solar wind parameters and geomagnetic indices for the event which occurred from 14:30 UT

71 to 17:40 UT on 27 August 2013. Following the enhanced southward IMF (Figure 1a), E_{SW} (Figure 1e) evidently increased at

72 ~15:53 UT and reached >2mV/m after 16:30 UT. As shown by AL and SYM-H indices (Figures 1f and 1g), the strong

73 southward IMF triggered a substorm, which occurred during the initial and main phases of a geomagnetic storm. Since the

74 large scale magnetospheric dawn-dusk convection electric field is produced mainly due to the penetration of E_{SW} (Huang et

75 al., 2006; Lei et al., 1981; Toffoletto and Hill, 1989), magnetospheric electric field is also expected to be enhanced during this

76 time interval.

77 Figures 2a-2g show the observation of Van Allen Probe A from 14:00 UT to 16:30 UT. The measurement of total electron

78 density (Figure 2a) with a high value (> 60 cm^{-3}) before 16:20 UT implies that the Van Allen Probe A was inside the duskside

79 plasmasphere during this time interval. Strong plasmaspheric hiss waves (Figures 2b-2e) were observed over 14:00-16:30 UT,

80 together with magnetosonic waves (MS) at low frequencies (below 90 Hz), whose ellipticity is close to zero and wave normal

81 angle is close to 90°. Figure 2e illustrates the angle between Poynting flux and ambient magnetic field. Here, 0° (180°) indicates

82 that the Poynting flux is parallel (antiparallel) to the magnetic field. Interestingly, the plasmaspheric hiss waves at different L

83 shells reveal different characteristics. At lower L shells ($L < 4.67$, prior to 15:00 UT), the Poynting flux of hiss waves is mainly

84 bidirectional in most times, which implies that the observed hiss waves may have mainly originated from the chorus waves

85 outside the plasmasphere and experienced multiple reflections inside the plasmasphere (Bortnik et al., 2008, 2009; Liu et al.,

86 2017a, 2017b). However, at higher L shells ($L > 4.67$, after 15:00 UT), the Poynting flux is mostly directed away from the

87 equator, the ellipticity of hiss is extremely high (> 0.9), and wave normal angles are very small ($< 15°$). All these features

88 imply that the hiss waves at higher L shells are likely locally amplified near the equatorial region (He et al., 2019; Kletzing et

89 al., 2014; Laakso et al., 2015; Su et al., 2018).

90 The energetic electron fluxes in different energies measured by MagEIS ($> \sim 30$ keV) and HOPE (11 keV-30 keV) are merged

91 and presented in Figure 2f. The electron minimum cyclotron resonant energies (E_{min}) for the lower cutoff frequency of

92 plasmaspheric hiss (marked by the black solid curves in Figures 2b-2e) are calculated and presented as the black curve in

93 Figure 2f. There is a clear characteristic separation between hiss waves at lower L shells ($L < 4.67$) and those at higher L shells

94 ($L > 4.67$). The calculated E_{min} is higher than the measured electron energies before 15:00 UT ($L > 4.67$), which suggests that

95 the hiss waves are hardly locally generated. By contrast, the E_{min} agrees well with the measured electron energies at higher L

96 shells ($L > 4.67$). It supports that the hiss waves at higher L shells may be locally amplified. Using measured electron pitch

97 angle distribution and plasma parameters, we calculate the convective linear growth rates for parallel-propagating whistler-

98 modes waves with various frequencies (Kennel and Petschek et al., 1966; Summers et al., 2009). The linear wave growth rate

99 (Figure 2g) shows positive values at higher L shells (> 4.67), and the frequency range of high positive growth rate agrees fairly

100 well with the hiss waves observed at higher L shells. At lower L shells ($< \sim 4.67$), only the high frequency portion shows the

101 positive growth rates, indicating local amplification. This feature is roughly consistent with the Poynting flux direction (Figure

102 2e), where only the high frequency portion ($>$ several hundred Hz) exhibits the Poynting flux directed away from the equator.

103 Figures 2h-2n show the observation of Van Allen Probe B from 16:00 UT to 18:20 UT. Van Allen Probe B passed through the

104 same region at ~ 2 h later than the observation by Probe A (Figures 2a-2g). At the same L shell, the change in total electron

105 density was very small. Interestingly, compared to the observation of Probe A (Figure 2f), there was a very clear decrease in

106 energetic electron fluxes at $> \sim 10$ keV at higher L shells (Figure 2m). Furthermore, the electron flux at $> \sim 25$ keV decreased

107 earlier and more significantly than that at $< \sim 25$ keV. At higher L shells, in association with the decrease in energetic electron

108 fluxes, the corresponding linear growth rate became much lower, especially at frequencies $< 0.1\ f_{ce}$. Except for the waves at

109 higher frequencies ($> 0.1\ f_{ce}$), which propagate away from the equator (Figure 2l), the Poynting flux of the plasmaspheric hiss

110 was bidirectional. Interestingly, linear growth rates (Figure 2n) show positive values for these high frequency hiss ($> 0.1\ f_{ce}$),

111 suggesting local amplification, which is consistent with their Poynting flux direction (Figure 2l). It is important to note that

112 the intensity of plasmaspheric hiss became very weak over the L shells of ~ 4.5-5.5. This suggests that the local amplification

113 of plasmaspheric hiss was reduced, owing to the decreased electron flux, which provides a source of free energy for hiss

114 amplification.

115 **4 Simulation of energetic electron flux**

116 Previous studies have reported that the plasmaspheric hiss on the dayside could become weaker or disappear following the

117 interplanetary shock arrival due to enhanced Landau damping which prevented chorus waves from entering the plasmasphere

118 (Su et al., 2015; Yue et al., 2017). In this study, the plasmaspheric hiss event on 27 August 2013 was observed on the duskside.

119 Although there were some variations in solar wind dynamic pressure, the attenuation of duskside plasmaspheric hiss wave

120 intensity at higher L shells is likely caused by the decrease of energetic electron fluxes which provide free energy for cyclotron

121 resonance. Since the timescale of energetic electron loss due to hiss-induced pitch angle scattering is 1 to 100 days (Ni et al.,

122 2013), the rapid loss in electron flux cannot be caused by the hiss wave scattering. After 15:53 UT, the enhanced southward

123 interplanetary magnetic field resulted in intense E_{SW} and triggered a substorm, which further enhanced the magnetospheric

124 electric field. The intense magnetospheric electric field can drive charged particles to move sunward and outward (Khazanov

125 et al., 2004), and lead to the significant decrease of energetic electron flux along the Van Allen Probes' orbit within a short

126 time.

127 Following Goldstein et al. (2003) and Goldstein et al. (2005a), we built a magnetospheric model for the electric potential. In

128 the model, except for the co-rotating electric potential Φ_{rot},

$$\Phi_{rot} = -C\frac{R_E}{R} \tag{1}$$

130   the major parts are the convection electric potential and SAPS potential. The convection electric potential Φ_{VS} is determined

131   by E_{SW},

$$\Phi_{VS} = -AE_{SW}R^2 \sin\varphi \, (6.6R_E)^{-1} \,, \tag{2}$$

133   where A is equal to 0.13, R is the geocentric distance, φ is the azimuthal angle, and R_E is the radius of the Earth. Following

134   Goldstein et al., (2003), we consider a time delay between the detected E_{SW} and its effect on magnetospheric electric field. In

135   this study, E_{SW} data from OMNI is delayed by ~5 minutes, which is shown in Figure 3a.

136   The SAPS associated with substorm can also evidently enhance the electric field near the duskside. From 15:16 UT to 15:22

137   UT, the horizontal flow speed V (and minimal convection) recorded by DMSP F17 at the magnetic local time (MLT) of ~17.2

138   (before the enhancement of southward IMF and onset of substorm) was small (Figure 3b). The SAPS on the equatorward side

139   of the auroral oval was not evident. Subsequently, the horizontal V recorded by DMSP F17 from 16:58 UT to 17:03 UT at

140   ~17.5 MLT (during the enhancement of southward of IMF and substorm) increased significantly with the peak flow speed >1

141   km/m, indicating a strong SAPS event (marked by two vertical dashed lines in Figure 3c).

142   In this study, the effect of SAPS on the magnetospheric equatorial electric potential Φ_S is calculated by,

$$\Phi_S(R,\varphi,t) = -F(R,\varphi)G(\varphi)V_S(t) \tag{3}$$

144   where $F(R,\varphi)$ is a function to describe the radial dependence.

$$F(R,\varphi) = \frac{1}{2} + \frac{1}{\pi}tan^{-1}[\alpha\{R - R_S(\varphi)\}] \tag{4}$$

146   where R_S indicates the radial distance where the peak radial electric field occurs.

$$R_S(\varphi) = R_S^0 \left(\frac{1+\beta}{1+\beta COS(\varphi-\pi)}\right)^\kappa \tag{5}$$

148   where α indicates the width of the peak,

$$\alpha = 0.15 + 0.65[1 + \cos\left(\varphi - \frac{7\pi}{12}\right)]. \tag{6}$$

150    $G(\varphi)$ is used to model the azimuthal dependence of the potential drop,

$$G(\varphi) = \cos^2\left[\frac{1}{2}(\varphi - \varphi_S)\right] \,. \tag{7}$$

152   We consider the SAPS potential with parameters $[\beta, \kappa, R_S^0, \varphi_S]=[0.97, 0.14, 5.2R_E, \pi/2]$.

153    $V_S(t)$ describes the time dependence of magnetospheric equatorial SAPS potential, which is

$$V_S(t) = 11[\exp\{-(t - 16.3)^2\}] + 38[\exp\{-4(t - 17.7)^2\}] \,, \tag{8}$$

155   where t is the UT in hour.

156   In order to compare the modelled and the actual electric fields, the modelled electric potential along the F17's orbits during

157   the intervals both from 15:16 UT to 15:22 UT and from 16:58 UT to 17:03 UT are calculated using a dipolar magnetic field,

158   as indicated by the red curves in Figure 3d and 3e, respectively. In addition, the actual F17 electric potentials relative to the

159   electric potential at MLAT~50° (assumed as 0 at ~50°) are indicated by the blue curves in Figures 3d and 3e, respectively. The

160   actual electric potentials are calculated through the integration of $V{\times}B$ along the F17's orbit, where B is the downward

161   component of geomagnetic field. Although there is a slight difference between the modelled and actual potentials, the potential

162   drop is quite close. It suggests that the potential drop is small before the enhancement of southward IMF (as shown in Figure

163   3d). However, the potential drop is large during the enhancement of southward IMF (as shown in Figure 3e), which implies

164   that the electric field dramatically strengthened. Furthermore, the modelled and detected magnetospheric electric fields in the

165   dawn-dusk direction along the trajectory of Probe A are indicated by the red and blue curves in Figure 3f, respectively. It

166   suggests that the modelled magnetospheric electric field is very similar to the observed electric field, and there is a clear trend

167   that the magnetospheric electric field varied following the enhancement of E_{SW}.

168   Using the modelled time-varying electric field, we simulate the evolutions of energetic electron distributions. Here the

169   geomagnetic field is assumed as a dipolar field and electron motion is assumed to be adiabatic. We calculate the drift velocity

170   as a combination of the velocity due to $E \times B$ drift, and the bounce-averaged velocity due to gradient and curvature drifts

171   (Roederer, 1970; Ganushkina et al., 2005). In this study, the evolution of electron flux distributions at lower energies from 11

172   to 21 keV and higher energies from 51 to 61 keV (representing energy <~25 keV and energy >~25 keV) is simulated,

173   respectively.

174   In order to obtain the initial electron flux distribution function, the observed flux distribution of energetic electrons (at each

175   energy channel measured by Probe A from ~14:00 UT to 16:10 UT) as a function of L shell is fitted with the summation of

176   several Maxwellian functions. And then, the fitted flux distribution is interpolated at 1 keV steps. The distribution achieved

177   by above method is considered as the initial energetic electron distribution. There may be a temporal evolution of energetic

178   electrons within the time interval from 14:00 UT to 16:10 UT. However, we consider that the variation during this time interval

179   is relatively smaller, because the E_{SW} is very low in most of this time interval. Moreover, the electron flux distribution is

180   assumed to be the same at different MLTs. Since the results of simulation for different initial pitch angles are similar, the

181   evolution of electrons with initial pitch angle at 45° is presented here. As shown in Figure 4a, the electrons at energies from

182   11 to 21 keV are assumed to be evenly distributed across all MLTs, and distributed along the L shells using a function presented

183   in Figure 2f. The simulation of energetic electron flux is initialized at 15:58 UT, when the delayed E_{SW} started to increase

184   (Figure 3a). The trajectory of the Van Allen Probes is denoted by the black curve. The evolved distribution at 17:15 UT is

185   shown in Figure 4b. Although the sunward motions of electrons could be seen both on the dayside and nightside, this trend is

186   more notable on the duskside. Furthermore, there is also an evident outward motion on the duskside. To explicitly display the

187   evolution of electron flux along the satellite orbit, the normalized percentage changes in modelled electron fluxes (at $L \sim 4.75$,

188   MLT ~ 17 and $L \sim 5.1$, MLT ~ 18) varying with time (staring at 15:58 UT) are shown in Figure 4c. The electron flux decreases

189   at both $L \sim 4.75$ and $L \sim 5.1$. In Figure 4c, the detected normalized variations of electron fluxes at the corresponding times

190   when Van Allen Probe B passed through are indicated by the vertical bars (17:04 UT for $L \sim 4.75$ and 17:26 UT for $L \sim 5.1$).

191   The evolution of electron flux at energies from 51 to 61 keV is shown in Figures 4d-4f, which exhibit a distinct slot region at

192    $L \sim 4$. After the evolution of 77 minutes, as presented in Figure 4e, the inner belt remains stable and changes little. However,

193   the outer belt on the duskside clearly moves farther away from the Earth and becomes apparently sparser. The slot region on

194   the duskside becomes much broader, where the Van Allen Probes travelled through. As shown in Figure 4f, the electron flux

195   at energy from 51 to 61 keV rapidly decreases. At $L \sim 4.75$ (5.1), the modelled flux decreases by 91% (83%), similar to the

196   observed electron flux decrease. The decreases of both the modelled and observed flux at the energies from 51 to 61 keV are

197   more significant than those at energies from 11 to 21 keV.

198   These simulation results indicate that the enhanced electric field during the enhanced convection and substorm redistributes

199   the energetic electron flux along the orbit of Van Allen Probes. Although there are stronger sunward and outward motions for

200   the electrons at lower energies (from 11 to 21 keV), the decrease of local electron flux along the orbit of Van Allen Probe is

201   slower than the decrease of electron flux at higher energies (from 51 to 61 keV).

5 Conclusions

203   In this paper, we report a hiss attenuation event during an enhanced convection and substorm event on 27 August 2013. In the

204   outer plasmasphere, with the decrease of energetic electron fluxes after the enhanced convection and substorm, the hiss wave

205   intensity became much weaker. The Poynting flux of hiss waves observed at higher L shells ($> \sim 4.67$) before the enhanced

206   convection and substorm was directed away from the equator, and the trend of the calculated linear wave growth rates is

207   consistent with the observed hiss wave intensification, both of which suggest that these hiss waves in the outer plasmasphere

208   are mainly locally amplified. The reduction of hiss wave intensity in the outer plasmasphere after the enhanced convection and

209   substorm may be mainly caused by the reduced fluxes of energetic electrons (tens of keV), which provide a source of free

210   energy for hiss amplification.

211   The evolution of electron fluxes during the time interval of enhanced magnetospheric electric field at different L shells is

212   modelled by test particle simulations based on the realistic electric field model including both convection electric field and

213   SAPS. The result of test particle simulation is consistent with the observed distribution of electron flux from Van Allen Probes,

214   showing decreased electron flux along the orbit of the Van Allen Probes after the enhanced convection and substorm. The

215   result of test particle simulation is consistent with the observed distribution of electron flux from Van Allen Probes, showing

216   decreased electron flux along the orbit of the Van Allen Probes after the enhanced convection and substorm. Furthermore, the

217   electron flux is highly energy dependent, the decline of electron flux at the energies from 51 to 61 keV is more significant than

218   that at energies from 11 to 21 keV. The electrons at energies from 11 to 21 keV have stronger sunward and outward motions,

219   because their velocities of gradient and curvature drift (rotation around the Earth) are lower. However, under the supplement

220   of electrons from lower L shells which are also owing to the convection, the electron fluxes around the orbit of Van Allen

221   Probe at these energies decrease slower. There is a distinct slot region of electrons at energies from 51 to 61 keV around $L \sim 4$.

222   The inner belt remains stable and changes little during the interval of evolution, because the motions of energetic electrons

223   within $L < 3.5$ are mainly controlled by the relatively stable co-rotating electric field and magnetic field in the substorm. By

224   contrast, under the action of enhanced convection electric field, the outer belt on the duskside clearly moves farther away from

225   the Earth. The extended slot region for the electrons covers the orbit of Van Allen Probe, which results in a significant decrease

226   of measured flux for the electrons at energies from 51 to 61 keV. The simulation results indicate that the enhanced electric

field causes the outward and sunward motions of energetic electrons, which lead to the observed hiss attenuation on the duskside. This study reveals the important role of magnetospheric electric field in the variation of energetic electron flux and the resultant hiss wave intensity.

Our simulation implies that the attenuation of hiss wave intensity is mainly due to the decrease of energetic electron fluxes, especially electrons at higher energies, in association with the enhanced magnetospheric electric field in response to solar wind and substorm activity. This suggests that the enhanced magnetospheric electric field may also contribute to the attenuation of chorus waves outside the plasmasphere, since tens of keV electrons provide a source of free energy for chorus wave excitation. The potential chorus attenuation, although unavailable from other satellite measurements during this event, is left as a further investigation.

Author contributions. The conceptional idea of this study was developed by HL and WL. HL wrote the paper, and WL revised it. QM, YN and ZY substantially helped with the analysis. AJB and XS contributed to the Van Allen Probe data processing. All authors discussed the results.

Competing interests. The authors declare that they have no conflict of interest.

References

Blake, J. B., et al.: The Magnetic Electron Ion Spectrometer (MagEIS) Instruments Aboard the Radiation Belt Storm Probes (RBSP) spacecraft, Space. Sci. Rev., doi:10.1007/s11214-013-9991-8, 2013.

Bortnik, J., R. M. Thorne, and N. P. Meredith: The unexpected origin of plasmaspheric hiss from discrete chorus emissions, Nature, 452, 62–66, doi:10.1038/nature06741, 2008.

Bortnik, J., W. Li, R. M. Thorne, V. Angelopoulos, C. Cully, J. Bonnell, O. Le Contel, and A. Roux: An observation linking the origin of plasmaspheric hiss to discrete chorus emissions, Science, 324, 775–778, doi:10.1126/science.1171273, 2009.

Burch, J. L: The magnetosphere, in Upper Atmosphere and Magnetosphere, edited by F. S. Johnson, chap.2, National Academy of Sciences, Washington, D. C., 1977.

258 Chan, K. W., and R. E. Holzer: ELF hiss associated with plasma density enhancements in the outer magnetosphere, J. Geophys.
259 Res., 81(13), 2267–2274, doi:10.1029/JA081i013p02267, 1976

260 Chen, L., Thorne, R. M., Bortnik, J., Li, W., Horne, R. B., Reeves, G. D., et al.: Generation of unusually low frequency
261 plasmaspheric hiss. Geophysical Research Letters, 41, 5702–5709, 2014

262 Draganov, A. B., Inan, U. S., Sonwalkar, V. S., & Bell, T. F.: Magnetospherically reflected whistlers as a source of
263 plasmaspheric hiss. Geophysical Research Letters, 19, 233–236, 1992

264 Ejiri, M.: Trajectory traces of charged particles in the magnetosphere, J. Geophys. Res., 83(A10), 4798–4810,
265 doi:10.1029/JA083iA10p04798, 1978.

266 Frank, L. A., Magnetospheric and auroral plasmas. A short survey of progress, Rev. Geophys. Space Physics, 13, 974‑989,
267 1975.

268 Funsten, H. O., et al.: Helium, Oxygen, Proton, and Electron (HOPE) Mass Spectrometer for the Radiation Belt Storm Probes
269 Mission, Space Sci. Rev., doi:10.1007/s11214-013-9968-7, 2013.

270 Ganushkina, N. Yu., Pulkkinen, T. I., and Fritz, T.: Role of substorm-associated impulsive electric fields in the ring current
271 development during storms, Ann. Geophys., 23, 579–591, https://doi.org/10.5194/angeo-23-579-2005, 2005.

272 Goldstein, J., B. R. Sandel, M. R. Hairston, and P. H. Reiff: Control of plasmaspheric dynamics by both convection and sub-
273 auroral polarization stream, Geophys. Res. Lett., 30(24), 2243, doi:10.1029/2003GL018390, 2003

274 Goldstein, J., B. R. Sandel, W. T. Forrester, M. F. Thomsen, and M. R. Hairston: Global plasmasphere evolution 22–23 April
275 2001, J. Geophys. Res., 110, A12218, doi:10.1029/2005JA011282, 2005a.

276 Goldstein, J., J. L. Burch, and B. R. Sandel: Magnetospheric model of subauroral polarization stream, J. Geophys. Res., 110,
277 A09222, doi:10.1029/2005JA011135, 2005b.

278 Green, J. L., Boardsen, S., Garcia, L., Taylor, W. W. L., Fung, S. F., & Reinisch, B. W.: On the origin of whistler mode
279 radiation in the plasmasphere. Journal of Geophysical Research, 110, A03201, 2005.

280 He, Z., Chen, L., Liu, X., Zhu, H., Liu, S., Gao, Z., & Cao, Y.: Local generation of high-frequency plasmaspheric hiss observed
281 by Van Allen Probes. Geophysical Research Letters, 46, 1141–1148, 2019.

282 Huang, C.-S., Sazykin, S., Chao, J., Maruyama, N., Kelley, M.C.: Penetration electric fields: efficiency and characteristic time
283 scale. Journal of Atmospheric and Solar–Terrestrial Physics, doi:10.1016/j.jastp.2006.08.016, 2006.

284 Kennel, C. F., and H. E. Petschek: Limit on stably trapped particle fluxes, J. Geophys. Res., 71(1), 1–28,
285 doi:10.1029/JZ071i001p00001, 1966.

286 Khazanov, G. V., M. W. Liemohn, T. S. Newman, M.-C. Fok, and A. J. Ridley: Magnetospheric convection electric field
287 dynamics and stormtime particle energization: Case study of the magnetic storm of 4 May 1998, Ann. Geophys, 22, 497–510,
288 2004.

289 Kletzing, C. A., et al.: The Electric and Magnetic Field Instrument Suite and Integrated Science (EMFISIS) on RBSP, Space
290 Sci. Rev., 179, 127–181, doi:10.1007/s11214-013-9993-6, 2013.

291 Kletzing, C., Kurth, W.S., Bounds, S. R., Hospodarsky, G.B., Santolik, O., Wygant, J. R., et al.: Evidence for significant local
292 generation of plasmaspheric hiss. Abstract SM14A-09 Presented at the 2014 AGU Fall Meeting, San Francisco, CA, December
293 15–19, 2014.

294 Laakso, H., Santolik, O., Horne, R., Kolmasová, I., Escoubet, P., Masson, A., & Taylor, M.: Identifying the source region of
295 plasmaspheric hiss. Geophysical Research Letters, 42, 3141–3149, 2015.

296 Lei, W., Gendrin, R., Higel, B., and Berchem, J.: Relationships between the solar wind electric field and the magnetospheric
297 convection electric field, Geophys. Res. Lett., vol. 8. doi 10.1029/GL008i010p01099, 1981.

298 Li, W., et al.: An unusual enhancement of low-frequency plasmaspheric hiss in the outer plasmasphere associated with
299 substorm-injected electrons, Geophys. Res. Lett., 40, 3798–3803, doi:10.1002/grl.50787, 2013.

300 Li, W., Q. Ma, R. M. Thorne, J. Bortnik, C. A. Kletzing, W. S. Kurth, G. B. Hospodarsky, and Y. Nishimura: Statistical
301 properties of plasmaspheric hiss derived from Van Allen Probes data and their effects on radiation belt electron dynamics, J.
302 Geophys. Res. Space Physics, 120, 3393–3405, doi:10.1002/2015JA021048, 2015a.

303 Li, W., L. Chen, J. Bortnik, R. M. Thorne, V.Angelopoulos, C.A.Kletzing, W.S.Kurth, and G. B. Hospodarsky: First evidence
304 for chorus at a large geocentric distance as a source of plasmaspheric hiss: Coordinated THEMIS and Van Allen Probes
305 observation, Geophys. Res. Lett., 42, 241–248, doi:10.1002/2014GL062832, 2015b.

306 Li, H., Z. Yuan, X. Yu, S. Huang, D. Wang, Z. Wang, Z. Qiao, and J. R. Wygant: The enhancement of cosmic radio noise
307 absorption due to hiss-driven energetic electron precipitation during substorms. J. Geophys. Res. Space Physics, 120,5393-
308 5407, doi: 10.1002/2015JA021113, 2015.

309 Liu, N., et al.: Simultaneous disappearances of plasmaspheric hiss, exohiss, and chorus waves triggered by a sudden decrease
310 in solar wind dynamic pressure, Geophys. Res. Lett., 44, 52–61, doi:10.1002/2016GL071987, 2017a.

311 Liu, N., Su, Z., Gao, Z., Reeves, G. D., Zheng, H., Wang, Y., & Wang, S.: Shock-induce disappearance and subsequent
312 recovery of plasmaspheric hiss: Coordinated observations of RBSP, THEMIS, and POES satellites. Journal of Geophysical
313 Research: Space Physics, 122, 10,421–10,435. https://doi.org/10.1002/2017JA024470, 2017b

314 Ma, Q., W. Li, R. M. Thorne, J. Bortnik, G. D. Reeves, C. A. Kletzing, W. S. Kurth, G. B. Hospodarsky, H. E. Spence, D. N.
315 Baker, J. B. Blake, J. F. Fennell, S. G. Claudepierre, and V. Angelopoulos: Characteristic energy range of electron scattering
316 due to plasmaspheric hiss, J. Geophys. Res. Space Physics, 121, 11, 737–11,749, doi:10.1002/2016JA023311, 2016.

317 Mauk, B. H., N. J. Fox, S. G. Kanekal, R. L. Kessel, D. G. Sibeck, and A. Ukhorskiy: Science objectives and rationale for the
318 Radiation Belt Storm Probes mission, Space Sci. Rev., 179, 3–27, doi:10.1007/s11214-012-9908-y, 2012.

319 Meredith, N. P., R. B. Horne, R. M. Thorne, D. Summers, and R. R. Anderson: Substorm dependence of plasmaspheric hiss,
320 J. Geophys. Res., 109, A06209, doi:10.1029/2004JA010387, 2004.

321 Meredith, N. P., R. B. Horne, S. A. Glauert, R. M. Thorne, D. Summers, J. M. Albert, and R. R. Anderson: Energetic outer
322 zone electron loss timescales during low geomagnetic activity, J. Geophys. Res., 111, A05212, doi:10.1029/2005JA011516,
323 2006.

Meredith, N. P., R. B. Horne, S. A. Glauert, and R. R. Anderson: Slot region electron loss timescales due to plasmaspheric hiss and lightning-generated whistlers, J. Geophys. Res., 112, A08214, doi:10.1029/2007JA012413, 2007.

Meredith, N. P., R. B. Horne, S. A. Glauert, D. N. Baker, S. G. Kanekal, and J. M. Albert: Relativistic electron loss timescales in the slot region, J. Geophys. Res., 114, A03222, doi:10.1029/2008JA013889, 2009.

Mishin, E. V., and V. M. Mishin: Prompt response of SAPS to stormtime substorms, J. Atmos. Sol. Terr. Phys., 69, 1233–1240, 2007.

Ni, B., J. Bortnik, R. M. Thorne, Q.Ma, and L. Chen: Resonant scattering and resultant pitch angle evolution of relativistic electrons by plasmaspheric hiss, J. Geophys. Res. Space Physics, 118, 7740–7751, doi:10.1002/2013JA019260, 2013.

Ni, B., et al. (2014), Resonant scattering of energetic electrons by unusual low-frequency hiss, Geophys. Res. Lett., 41, 1854–1861, doi:10.1002/2014GL059389, 2013.

Parrot, M., and F. Lefeuvre: Statistical study of the propagation characteristics of ELF hiss observed on GEOS 1, inside and outside the plasmasphere, Ann. Geophys., 4, 363–384, 1986.

Rich, F. J. and Hairston, M.: Large-scale convection patterns observed by DMSP: J. Geophys. Res., 99, 3827–3844.

Russell, C. T., R. E. Holzer, and E. J. Smith (1969), OGO 3 observations of ELF noise in the magnetosphere, 1. Spatial extent and frequency of occurrence, J. Geophys. Res., 74(3), 755–777, doi:10.1029/JA074i003p00755, 1994.

Roederer, J. G.（1970). Dynamics of geomagnetically trapped radiation, Springer-Verlag, New York, 36

Shi, R., Li, W., Ma, Q., Green, A., Kletzing, C. A., Kurth, W. S., et al.: Properties of whistler mode waves in Earth's plasmasphere and plumes. Journal of Geophysical Research: Space Physics, 124, 1035–1051. https://doi.org/10.1029/2018JA026041, 2019.

Spence, H. E. et al.: Science Goals and Overview of the Energetic Particle, Composition, and Thermal Plasma (ECT) Suite on NASA's Radiation Belt Storm Probes (RBSP) Mission, Space. Sci. Rev., 179 (1), 311-336, doi:10.1007/s11214-013-0007-5, 2013.

Su, Z., F. Xiao, H. Zheng, and S. Wang: CRRES observation and STEERB simulation of the 9 October 1990 electron radiation belt dropout event, Geophys. Res. Lett., 38, L06106, doi:10.1029/2011GL046873, 2011.

Su, Z., et al.: Disappearance of plasmaspheric hiss following interplanetary shock, Geophys. Res. Lett., 42, 3129–3140, doi:10.1002/2015GL063906, 2015.

Su, Z., Liu, N., Zheng, H., Wang, Y., & Wang, S.: Large-amplitude extremely low frequency hiss waves in plasmaspheric plumes. Geophysical Research Letters, 45, 565–577, 2018.

Summers, D., R. Tang, and R. M. Thorne: Limit on stably trapped particle fluxes in planetary magnetospheres, J. Geophys. Res., 114, A10210, doi:10.1029/2009JA014428, 2009.

Summers, D., Y. Omura, S. Nakamura, and C. A. Kletzing: Fine structure of plasmaspheric hiss, J. Geophys. Res. Space Physics, 119, 9134–9149, doi:10.1002/2014JA020437, 2014.

Thorne, R. M., E. J. Smith, R. K. Burton, and R. E. Holzer: Plasmaspheric hiss, J. Geophys. Res., 78(10), 1581–1596, doi:10.1029/JA078i010p01581, 1973.

358 Thorne, R. M., S. R. Church, and D. J. Gorney: On the origin of plasmaspheric hiss—The importance of wave propagation
359 and the plasmapause, J. Geophys. Res., 84, 5241–5247, doi:10.1029/JA084iA09p05241, 1979.

360 Thorne, R. M., et al.: Evolution and slow decay of an unusual narrow ring of relativistic electrons near L ~ 3.2 following the
361 September 2012 magnetic storm, Geophys. Res. Lett., 40, 3507–3511, doi:10.1002/grl.50627, 2013.

362 Toffoletto, F. R., and T. W. Hill, Mapping of the solar wind electric field to the Earth's polar caps, J. Geophys.
363 Res., 94, 329, 1989.

364 Wygant, J. R., et al.: The electric field and waves instruments on the Radiation Belt Storm Probes mission, Space Sci. Rev.,
365 179, 183–220, doi:10.1007/s11214-013-0013-7, 2013.

366 Yuan, Z., Y. Xiong, Y. Pang, M. Zhou, X. Deng, J. G. Trotignon, E. Lucek, and J. Wang: Wave-particle interaction in a
367 plasmaspheric plume observed by a Cluster satellite, J. Geophys. Res., 117, A03205, doi:10.1029/2011JA017152, 2012.

368 Yue, C., Chen, L., Bortnik, J., Ma, Q., Thorne, R. M., Angelopoulos, V., Li, J., An, X., Zhou, C., Kletzing, C., Reeves, G. D.,
369 & Spence, H. E.: The characteristic response of whistler mode waves to interplanetary shocks. Journal of Geophysical
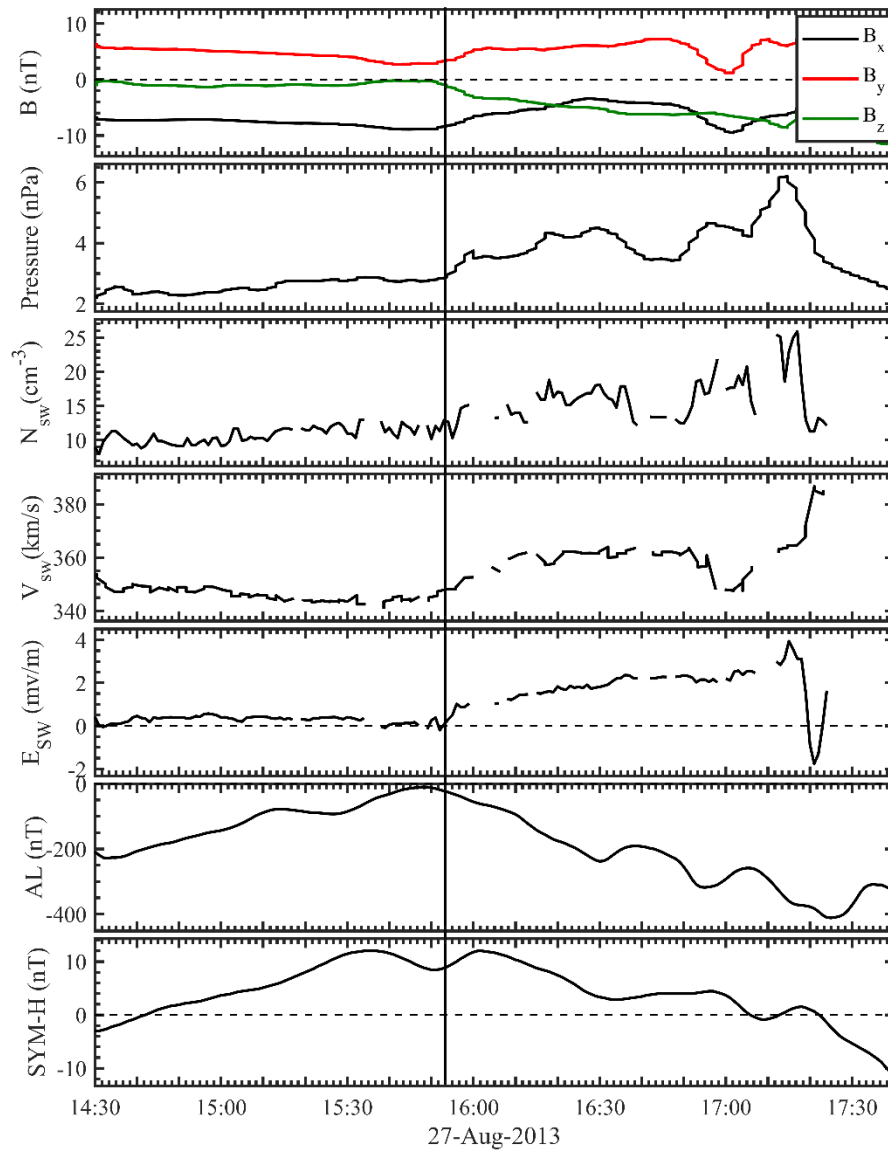370 Research: Space Physics, 122, 10,047– 10,057, 2017.

371
372
373
374
375
376
377
378
379
380
381

382

Figure 1. Solar wind and geomagnetic parameters from 14:30 UT to 17:40 UT on 27 August 2013. (a) Three components of IMF in the GSM coordinate. (b) Solar wind dynamic pressure, (c) proton density, (d) solar wind velocity, and (e) convection electric field of solar wind. (f) AL index and (g) SYM-H index. The vertical line indicates the time when the solar wind convection electric field started to increase.
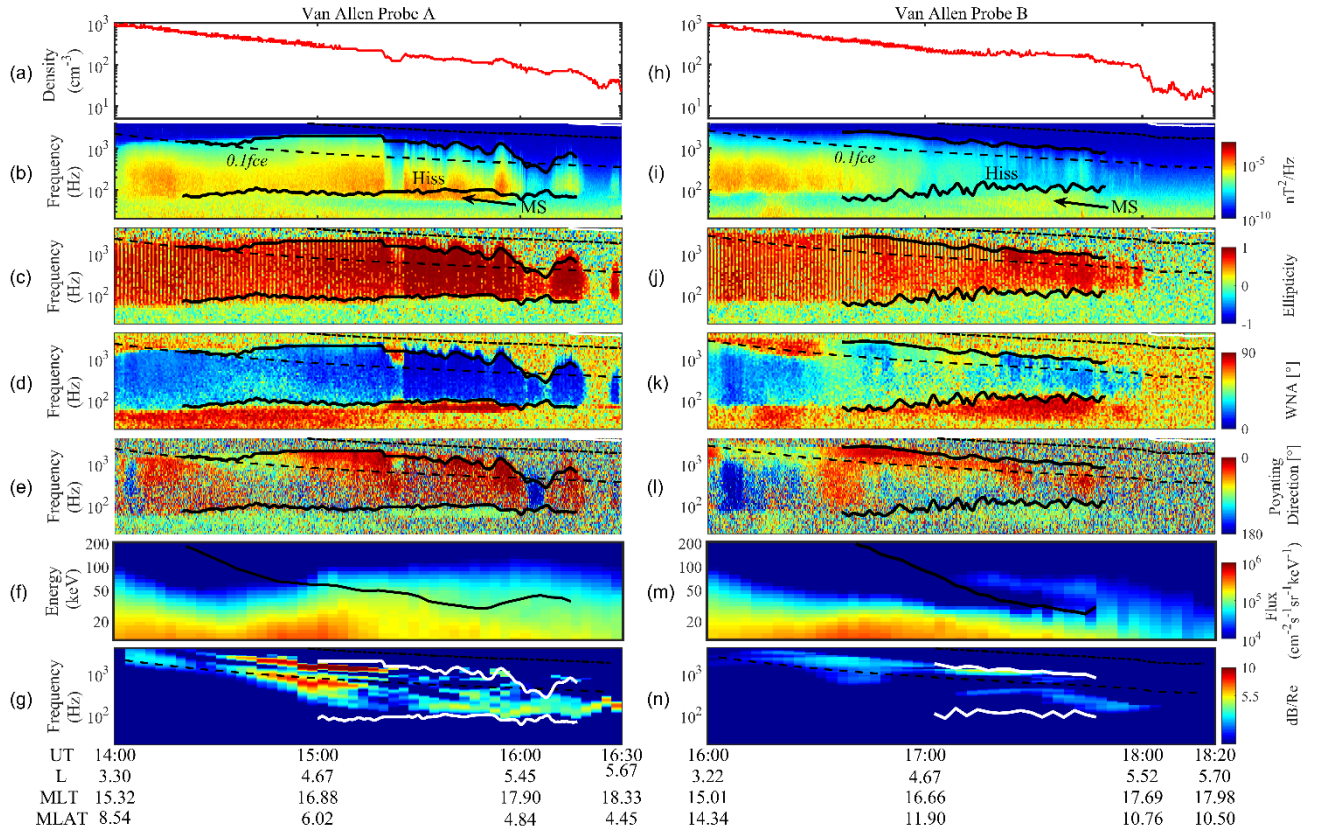
387
Figure 2. Overview of observations from Van Allen Probes A (left) over 14:00–16:30 UT and B (right) over 16:00–18:20 UT on 27 August 2013. (a) Total electron density. (b) Magnetic spectral density, where the black dashed line represents 0.1 f_{ce}., the black solid lines indicate the lower and upper cutoff frequencies of hiss waves. (c) Ellipticity, (d) wave normal angle, (e) the angle between Poynting flux and ambient magnetic field. (f) Omnidirectional electron fluxes from MagEIS and HOPE, where the black solid curve indicates the E_{min} corresponding to the lower cutoff frequency of the observed hiss. (g) Convective linear wave growth rates calculated for various frequencies, where the white solid lines represent lower and upper cutoff frequency of the observed hiss waves while $L>4.67$. (h-n) The same as Figure 2a-2g, but for the Van Allen Probe B observation.

14

395
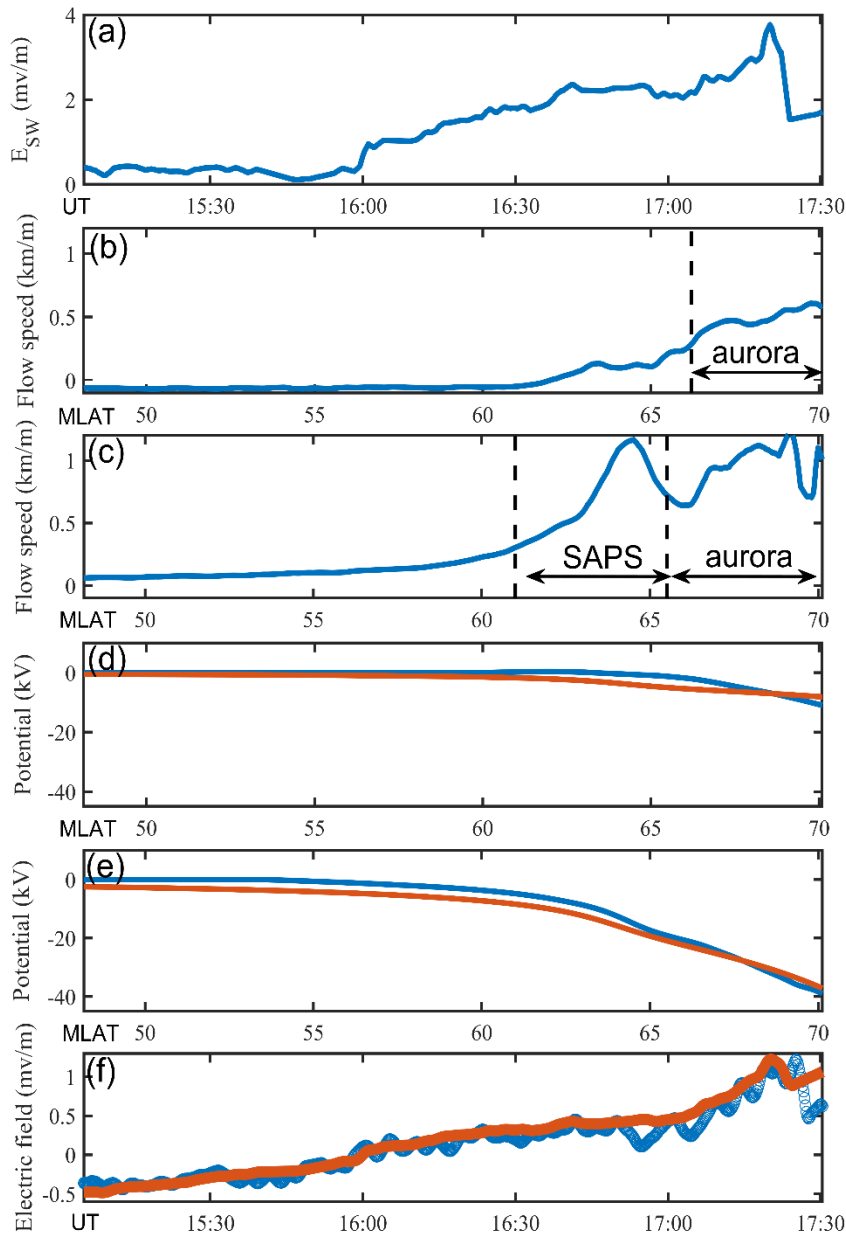
Figure 3. (a) The E_{SW} data from OMNI, but delayed by 5 min. (b) The flow speed detected by DMSP F17 from 15:16 UT to
15:22 UT at MLT ~ 17.2 h. (c) The flow speed detected by DMSP F17 from 16:58 UT to 17:03 UT at MLT ~ 17.5. The SAPS
region is indicated by the two vertical dashed lines. (d) The DMSP measured electric potential (blue curve), and the modelled
electric potential (red curve) from 15:16 UT to 15:22 UT. (e) The same as Figure 3d, but from 16:58 UT to 17:03 UT. (f) The
measured electric field in the dawn-dusk direction by Van Allen Probe A (blue curve), and the modelled electric field along
the trajectory of Van Allen Probe A (red curve).
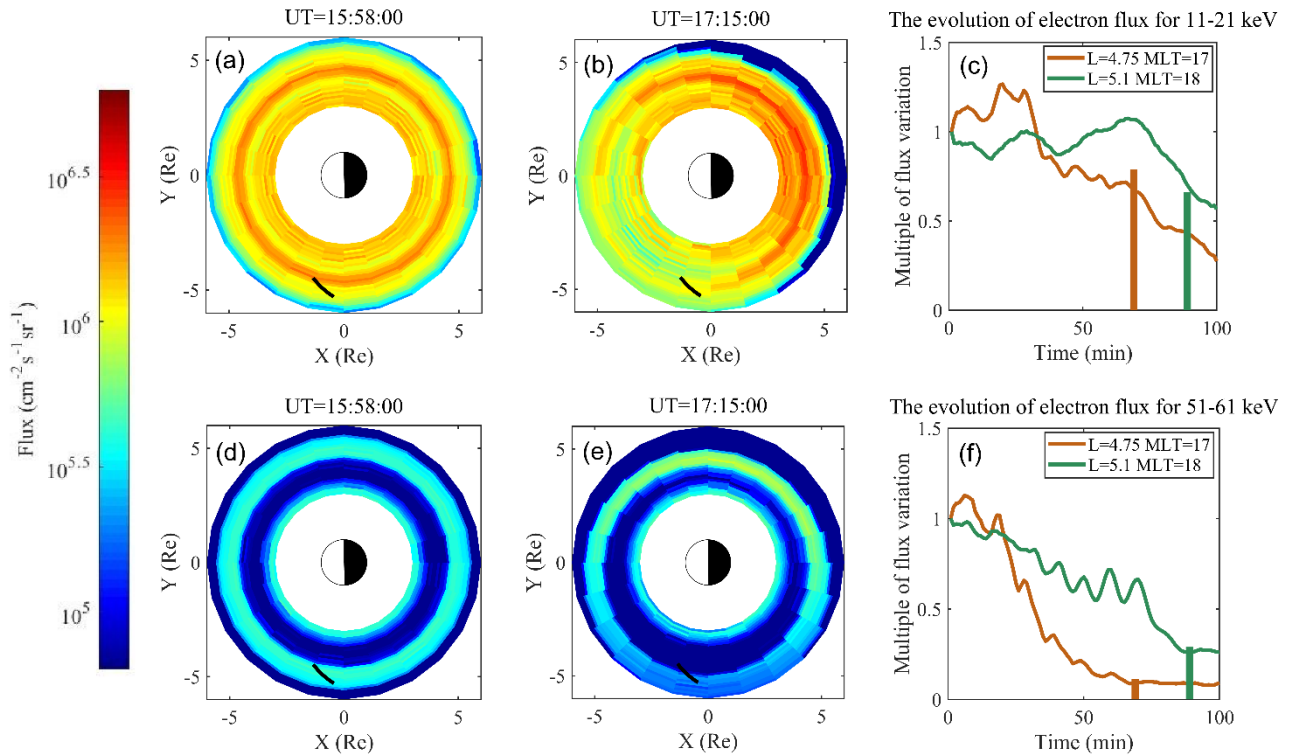
402

403 **Figure 4.** The comparison between the observed and simulated electron flux. (a) The simulation of electron flux distribution
404 with energies from 11 to 21 keV at 15:58 UT. The trajectory of the Van Allen Probes is indicated by the black solid curve. (b)
405 The evolved electron distribution with initial energies from 11 to 21 keV at 17:15 UT. (c) The normalized variations of electron
406 fluxes with the energies from 11 to 21 keV as a function of time after 15:58 UT at $L \sim 4.75$ ($L \sim 5.1$) are indicated by the brown
407 (green) curves. The vertical bars indicate the detected normalized variation of electron fluxes at the corresponding times when
408 Van Allen Probe B passed through $L \sim 4.75$ ($L \sim 5.1$). (d-f) The same as Figures 4a-4d, but for the electrons with the initial
409 energies from 51 to 61 keV.

410